The Astrophysical Journal Supplement Series, 149:365–373, 2003 December

A CATALOG OF BRIGHT FILAMENTARY STRUCTURES IN THE INTERSTELLAR MEDIUM

Tom Jackson
Princeton University Observatory, Princeton, NJ 08544; tsj5@pantheon.yale.edu

and

Michael Werner and T. N. Gautier III
Jet Propulsion Laboratory, MS 264-767, 4800 Oak Grove Drive, Pasadena, CA 91109;
mwerner@sirtfweb.jpl.nasa.gov, Thomas.N.Gautier@jpl.nasa.gov
Received 2003 April 1; accepted 2003 July 14

ABSTRACT

We present a listing of prominent filamentary structures in the interstellar cirrus, selected with an eye toward current and planned far-infrared and submillimeter polarimetry facilities. The filaments were identified on the 100 μm plates of the *IRAS* Sky Survey Atlas (ISSA), using a computer vision algorithm that is unbiased with respect to source intensity. Our catalog is two-tiered: the selection criteria in the Galactic plane are based on the sensitivity limits of airborne polarimeters such as the proposed HALE instrument for SOFIA, and away from the plane the limits are dictated by the sensitivities of balloon-borne cosmic microwave background experiments, such as BOOMERanG and MAXIMA. Infrared detector technology is currently at the point where detecting the polarization of the interstellar cirrus is feasible, and we hope this catalog will assist any experimenter undertaking this task.

Subject headings: catalogs — infrared: ISM — ISM: structure — methods: data analysis — techniques: image processing

1. INTRODUCTION

The Galactic magnetic field makes a major contribution to the pressure balance in the interstellar medium (ISM) and plays a significant role in the formation and motion of interstellar clouds (Beck et al. 1996). The value of this information is offset by the difficulty of measuring astrophysical magnetic fields; polarimetric measurements offer the best way of accomplishing this inside our Galaxy (Zweibel 1996). Polarization of transmitted starlight exploits differential extinction due to the alignment of nonspherical interstellar dust grains with the magnetic field axes. The complementary technique of far-infrared and submillimeter ($\sim$50 μm to $\sim$1 mm) polarimetry relies on the fact that elongated grains emit more efficiently with the electric vector along the long axis. The far-infrared polarization is on average a few percent but has been observed to be over 10% in places (Hildebrand et al. 2000).

Many of the early far-infrared studies were done on molecular clouds whose very density makes any conclusions about the magnetic field suspect: these clouds are products of gravitational collapse, which may have distorted the existing field lines, and turbulent internal gas motions can obscure what is really going on—in addition, the polarization from dust in one part of the cloud may be altered by other grains along the line of sight (Hildebrand et al. 2000).

To make good use of far-infrared polarimetry to map the Galactic magnetic field and to understand the interaction between the field and the ISM, simpler situations must be examined that will give less ambiguous information about the magnetic field. One way to accomplish this is by looking at the least dense component of the ISM possible—namely, the "infrared cirrus," extended low-level emission so named because of its resemblance to Earthly cirrus clouds. The cirrus has been resolved into filamentary structures on many length scales (Gautier et al. 1992; Verschuur 1994) that may be shaped in large part by magnetic effects. By studying linear, untangled filaments we can be more confident that the measured polarization reflects the actual nature of both the magnetic field and the grain alignment efficiency and mechanisms. In addition, we can test predictions concerning the polarization of an interstellar filament such as those presented by Fiege & Pudritz (2000).

Improvements in infrared detector technology have made polarimetry of the cirrus feasible, and proposals have recently been made by a number of groups for such studies (Novak et al. 1999; Clemens et al. 2000; Laureijs, Lemke, & Liljeström 1994). In addition, at the time of this writing several experiments to measure the polarization of the cosmic microwave background at wavelengths near 1 mm are being readied. It has already been demonstrated that these instruments are able to detect thermal radiation from high-latitude clouds with a resolution approaching that of *IRAS* (Masi et al. 2001), and our estimates show that they can feasibly expect to detect polarization of the cirrus at roughly a 10% level. Therefore, we present a catalog of regions of the cirrus most suited to polarimetry in the hopes of fostering advances in our state of knowledge about the Galactic magnetic field and its role in the ISM; the filaments in our catalog may also be useful targets for demonstrating the performance of the CMB polarimetry experiments if they are highly polarized, as we suspect.

We present three catalogs covering $|b| > 20°$, $|b| < 20°$ and the Large Magellanic Cloud, each constructed according to different criteria. Rather than select our targets by eye, in order to avoid bias in our catalog we present a pattern recognition algorithm for identifying filamentary structures on the *IRAS* Sky Survey Atlas plates. To make our selection more relevant to current experiments, our criteria for the Galactic plane catalog are chosen based on sensitivity estimates of airborne polarimeters such as HALE, and the criteria for the Galactic pole catalog are based on the sensitivity of the BOOMERanG and MAXIMA instruments. In

addition to brightness cutoffs, we make cuts on filament straightness and contrast with background emission.

2. METHODS

2.1. *Data*

The input images we used came from the *IRAS* sky survey atlas (ISSA) (Wheelock et al. 1994), a data product that presents the large-scale emission measured by *IRAS* over all of the sky with the zodiacal foreground removed. The ISSA data are formatted as 500×500 pixel FITS files each corresponding to an area of the sky $12.^{\circ}5$ square. Although cirrus is present to some extent in all of the *IRAS* wavelength bands, it is by far most apparent in the 100 μm band, which comes closest to sampling the peak of the $\sim$20 K blackbody approximating the thermal emission of the dust grains. We used the co-added images in this band in order to obtain a better signal-to-noise ratio. The resolution of the 100 μm data is $5'$, which is well sampled by the ISSA pixel size of $1.'5$.

Schlegel, Finkbeiner, & Davis (1998) have produced an improved calibration of the ISSA data based on the *COBE* results. The effective resolution of the Schlegel et al. (1998) baseline corrected 100 μm images is $6.'1$. Because the ISSA data have a relatively large zero point drift on scales of a degree or more, we used the Schlegel et al. images instead of the ISSA data for reporting the 100 μm fluxes and as a basis for extrapolating the *IRAS* results to submillimeter wavelengths. On the other hand, we use the ISSA data for identifying the filaments in the first place because of its slightly higher resolution and because our procedure for finding filaments is insensitive to the flux zero point. Since the typical width of a filament is much smaller than the characteristic size of the zero point fluctuations, we can be confident that the fluctuations in the ISSA data will not affect the results we obtain.

Based on the Schlegel et al. (1998) map and a temperature model for the dust grains, it becomes possible to extrapolate the measured intensity to other wavelengths, a procedure that is carried out in Finkbeiner, Davis, & Schlegel (1999). We make use of their routines to extrapolate the 100 μm brightness to wavelengths used by operational or proposed polarimeters. We use the two-component dust model corresponding to their best-fit parameters (model 7 in the paper previously cited). The results of Masi et al. (2001) confirm that this extrapolation is accurate for regions of diffuse cirrus[1] to the limit of the noise level of the BOOMERanG instrument. The thermal emission from large grains that these procedures model and that *IRAS* observed is predicted to be dominant for frequencies greater than 100 GHz. Therefore, we are confident in our ability to predict the filament brightness at 340 GHz, as is done below. Below 100 GHz, more exotic emission mechanisms from very small particles come into play (Lazarian & Draine 2000; Leitch et al. 1997).

2.2. *Algorithm*

The algorithm we use to select filaments follows the approach set forth in Lindeberg (1996, 1998). The algorithm uses a differential geometric formalism: the image is treated as a two-dimensional surface embedded in three dimensions by interpreting its brightness values as height. Bright filamentary structures can then be thought of as mountain ridges in this topographic analogy.

As a matter of notational convenience we represent directional derivatives as follows, with I being the intensity values of the image:

$$I_x = \frac{\partial I}{\partial x};\ \text{in general},\ I_v = \hat{\boldsymbol{v}} \cdot \nabla I\ , \tag{1}$$

$$I_{xx} = \frac{\partial^2 I}{\partial x^2};\ \text{in general},\ I_{uv} = \hat{\boldsymbol{u}} \cdot \nabla(\hat{\boldsymbol{v}} \cdot \nabla I)\ . \tag{2}$$

The Hessian matrix,

$$\mathbf{H} = \begin{pmatrix} I_{xx} & I_{xy} \\ I_{xy} & I_{yy} \end{pmatrix}, \tag{3}$$

is a quadratic form defined at each point of this surface. The second fundamental form of differential geometry in this basis is simply the Hessian multiplied by the scalar $(1 + |\nabla I|^2)^{-1/2}$ at each point (Koenderink 1990). The eigenvectors of the resultant matrix give the directions of principal curvature, which are the directions of maximum and minimum curvature of the local second-order approximation to the surface at the given point. The corresponding eigenvalues give the magnitude of the curvatures in those directions.

The Hessian's eigenvectors will be orthogonal as long as the matrix is nonsingular, a condition violated only at umbilic points, isolated (in our application) locations at which the geometry is locally spherical (and hence $I_{xx} = I_{xy} = I_{yy}$). In practice such points were not an issue, so to obtain the principal curvature directions we could simply define an angle

$$\beta = \frac{1}{2}\tan^{-1}\frac{2I_{xy}}{I_{xx} - I_{yy}} \tag{4}$$

through which the (x, y) axes are rotated. The derivative operators in the directions of principal curvature are then defined by

$$\partial_p = \sin\beta\frac{\partial}{\partial x} - \cos\beta\frac{\partial}{\partial y}\ , \tag{5}$$

$$\partial_q = \cos\beta\frac{\partial}{\partial x} + \sin\beta\frac{\partial}{\partial y}\ . \tag{6}$$

The principal curvature axes are defined so as to make the cross derivative I_{pq} uniformly zero: all second-order behavior of the surface can be thought of as some combination of curvature along these axes. The conditions satisfied by a point on the crest of a ridge are then

$$|I_{pp}| > |I_{qq}|,\ I_{pp} < 0,\ I_p = 0\ , \tag{7}$$

where without loss of generality we take p to point across the ridge. Respectively, these state the requirements that the curvature across the ridge is greater than curvature along the ridge axis, that the point in question lies on a ridge and not a valley, and that the point lies on the crest of the ridge instead of on its sides. Note that these are conditions on the signs of derivatives of the pixel intensities, and so these criteria are insensitive to shifts in the zero point of the image as well as the scale of intensities.

[1] Denser molecular clouds are cooler and deviate from the assumed dust model.

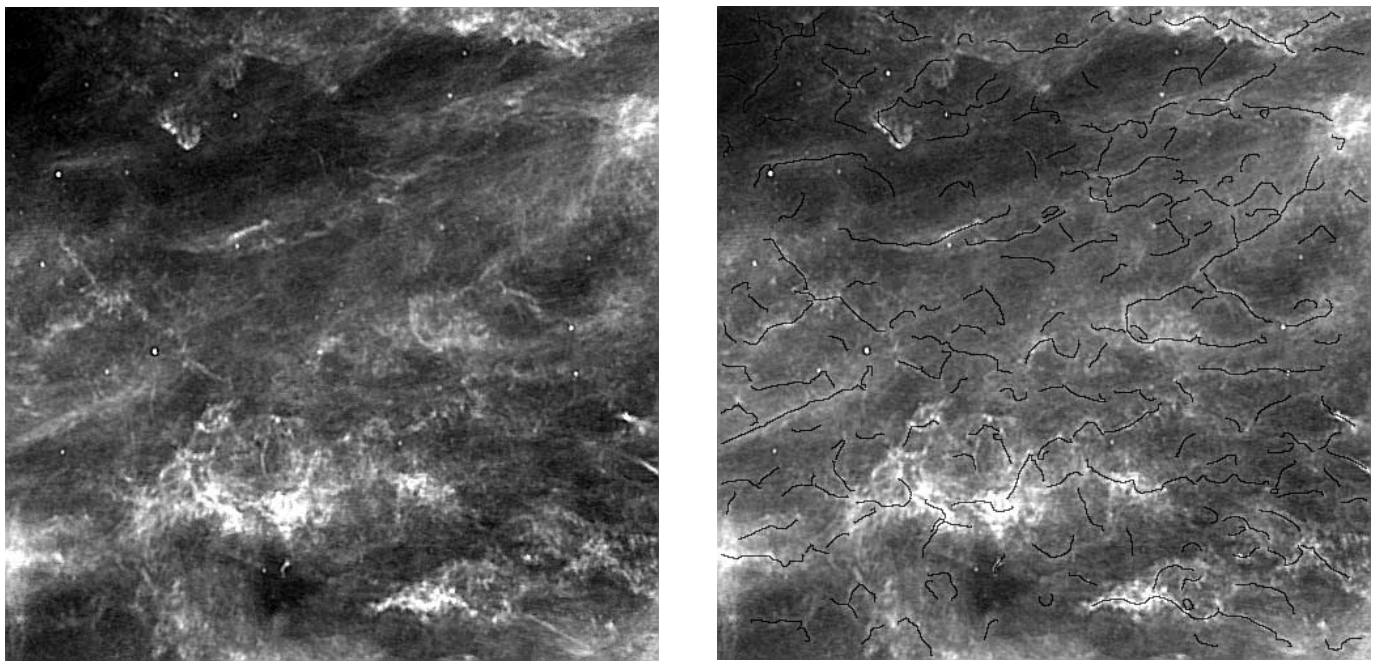

FIG. 1.—Performance of the filament finding algorithm on ISSA plate 001 at the south celestial pole. The left-hand picture shows the input data. On the right is the same data with the filaments overlaid in black. The strengths and weaknesses of the algorithm are discussed in the text.

The first step in our algorithm was to smooth the ISSA images with a Gaussian filter of width 4 pixels (6′). This procedure helps control the noise in the data, which otherwise could upset the stability of the derivative calculation, without much degradation of the 5′ ISSA spatial resolution.

The derivatives were calculated by finite difference methods on the pixels of the ISSA data. This produces derivatives in the local pixel coordinate system of the gnomonic projection used in the ISSA plates. We expect that this simplification poses no problems for our purposes.

After calculating the derivatives defined above, we prepared for each ISSA plate three new data sets in which the values of I_p, I_{pp}, and I_{qq} were associated with each pixel. We analyzed these arrays as though they were images, using the following procedure. First, we found the positions of pixels with zero I_p by using IDL's "CONTOUR" procedure on the I_p array to define the contour $I_p = 0$ and thus to identify the list of pixels with $I_p = 0$. We then applied the second derivative sign conditions as a binary mask on the list of points, which cut the continuous contour into many pieces: the detected filaments. The different filaments were labeled by using IDL's "LABEL_REGION" procedure on the binary mask. The LABEL_REGION procedure takes as input a binary image and assigns each connected group of nonzero pixels a different ID number. Each portion of the $I_p = 0$ contour that intersected a given labeled region of the binary mask was recorded as a distinct filament.

Some ISSA input data and the resulting detected filaments are shown in Figure 1. This field at the south equatorial pole shows considerable filamentary structure, which is picked out by our algorithm. The identified filaments correspond closely with structure picked out by eye. The application of the second derivative sign conditions and subsequent labeling by LABEL_REGION is well behaved and not very many long filaments are cut into smaller pieces. The filament finding algorithm finds many reasonable looking filaments that were not included in our catalog. For example, none of the filaments in Figure 1 were included in the final catalog, as the stringent brightness and contrast criteria set for the catalog exclude most of the candidate filaments in this and other regions. We believe that this restriction is reasonable since this catalog is intended to include bright candidate filaments for polarization measurements by the current generation of instrumentation and we expect that shortcomings of our detection method (see § 4) will likely be aggravated for dimmer filaments.

The coordinates of the contour points were in units of pixels from the origin of the ISSA plate, which were converted to epoch 1950 equatorial coordinates using the relation given in Beichman et al. (1988). The equatorial coordinates were converted to Galactic coordinates as input to Finkbeiner, Davis and Schlegel's extrapolation routines, which estimate the 340 GHz brightness of the filaments. These IDL routines take a position in Galactic coordinates, look up the corresponding position on their all-sky maps, and using those values and the results in Finkbeiner et al. (1999) return the extrapolated intensity at a given wavelength at that point.

All tabulated quantities other than the curvature and contrast scores (described below)—lengths, brightnesses, and positions—are calculated from the Schlegel, Finkbeiner, & Davis data for reasons noted in the previous section. The curvature and contrast scores are intended to be qualitative descriptors of how the filament appears in the ISSA data, and so are calculated from the uncorrected ISSA data.

Further discussion of the features of the algorithm is given in § 4.

3. RESULTS

The ridge detection algorithm was run on each of the 430 co-added 100 μm ISSA plates. No attempt was made to

match up filaments across plate boundaries or remove features that were duplicated due to the plates' overlap.

We have made use of two rudimentary measures of the shape of a filament: a curvature measure designed to weed out twisted or complicated filaments, and a contrast measure designed to approximate the degree to which a filament stands out against local background emission. The curvature measure is simply defined as the ratio of the endpoint-to-endpoint distance to the arc length of the filament and hence ranges from 0 to 1, with the straightest features having the higher ratio. The contrast measure is defined as

$$\partial_{pp}[\log I] = \frac{I_{pp} I - I_p^2}{I^2} = \frac{I_{pp}}{I} \tag{8}$$

on the filament ridge where I_p is zero. The quantity I_{pp} measures the curvature perpendicular to the filament axis and so is responsive to the difference between the filament brightness and the brightness of background regions. The choice of the function $(\log I)_{pp}$ was made to make the contrast measure agree with the judgments the eye makes: a contrast cut based on I_{pp} alone appears to be biased toward brighter filaments. The contrast score was computed from the uncorrected ISSA plates by averaging the contrast measure along the filament. This should not introduce significant bias, since the zero point fluctuations in the ISSA calibration occur on much larger scales than the finite differencing operation involved in calculating I_{pp}. As discussed further in § 4.2 below, we did not attempt to use this information to subtract background emission from the observed filament brightnesses: model brightness profiles of filamentary clouds exist (Fiege & Pudritz 2000), but attempting to fit a profile convolved with the irregular point spread function of *IRAS* to objects at the resolution limit would yield results of limited reliability.

When we speak of "the brightness of a filament" here and in the tables, we specifically refer to the mean intensity of all pixels that have been identified as part of that filament. Although filamentary structures may be found on virtually all of the ISSA plates, their brightness tends to follow the density of dust on broad scales—i.e., the brightest filaments are found in the regions of brightest emission on the plates: the Galactic plane, the ρ Ophiucii and Orion star-forming regions, etc. Brightness cutoffs are then effectively latitude cutoffs, which led us to develop a two-tiered selection scheme. Sources out of the plane of the Galaxy are selected so as to be detectable with balloon-borne CMB instruments and those in the plane detectable with dedicated airborne polarimeters.

The brightness criterion for the high-latitude catalog ($|b| > 20°$; Table 1) was that the extrapolated[2] ΔT at a frequency of 340 GHz be greater than 3 mK. This represents our estimate of the lowest flux at which one could hope to detect polarized emission at the 10% level with one of the current balloon-borne CMB experiments, based on the noise levels of the BOOMERanG instrument as shown in Masi et al. (2001). The additional requirements were an arc length greater than 30′, a curvature measure greater than 0.75 (the median is roughly 0.61), and a contrast measure greater than the median value. Because much of the observation time of CMB experiments is spent as far out of the plane of the Galaxy as possible, for $|b| > 40°$ the length and curvature criteria are dropped and *all* sources are admitted provided they satisfy the brightness requirement.

The criteria for the Galactic plane catalog ($|b| < 20°$; Table 2) were the same, except the brightness cutoff was changed to require that the Schlegel et al. (1998) baseline-corrected 100 μm flux be between 100 and 500 MJy sr^{-1}. The lower limit comes from our estimates of detection limits with airborne instruments such as the proposed HALE polarimeter for SOFIA, and the upper bound is placed out of a need to avoid the dense molecular clouds whose complexity motivated this work in the first place. Our HALE estimate assumes that the filament illuminates roughly 100 $8'' \times 8''$ pixels during an integration time of one hour (Novak et al. 1999). These criteria yield 83 sources in the high-latitude catalog and 47 sources in the plane catalog.

Regions containing the Large and Small Magellanic Clouds were masked out and treated separately. Sources with $275 < l < 285$ and $-37 < b < -30$ were assumed to be associated with the LMC and those with $300 < l < 307$ and $-47 < b < -42$ were considered to be part of the SMC. The selection criteria for these areas was the same as for the high-latitude region, except that the length requirement was dropped due to the difference in angular scale between Galactic and extragalactic structures. Ten sources satisfying these criteria were found in the LMC and none in the SMC and are listed in Table 3.

The locations of sources in all three subcatalogs are plotted in Figure 2.

4. DISCUSSION

4.1. *Algorithm*

Appleton, Siqueira, & Basart (1993) developed a filtering routine for the identification of interstellar cirrus based upon its behavior under repeated morphological processes. Their findings are probably related to the fractal structure of the clouds, but their algorithm does not specifically recognize filamentary features. For an image processing application such as ours, the Lindeberg algorithm is the most appropriate ridge detector among several procedures that exist in the literature (López 1999).

An inspection of the Lindeberg algorithm's output shows that the filament structure it returns is frequently at odds with what the eye sees: filaments are frequently broken up into shorter pieces, and the detection of superimposed structures is handled poorly, as one can see in Figure 1. The former problem is attributable to the limited resolution of the binary mask used in evaluating the sign conditions, while the latter problem stems from the mathematical definition we have adopted: where two ridges cross, they momentarily cease to be identifiable in terms of curvature perpendicular to the ridge axis. In other words, the problem is with our condition $I_p = 0$; for example, there is no way the algorithm can correctly identify the hypothetical situation in which three ridges meet at a point (zero crossings cannot end at a point). The problem of broken filaments is not serious in this catalog, but a more versatile ridge detector could possibly define ridges through phase discontinuities in some angular quantity and improve this performance.

These omissions are beside the point for the more limited purposes of this paper. We do not need to recover the

[2] The quantity ΔT as used here and in the tables is identical to the thermodynamical ΔT defined by Finkbeiner et al. (1999).

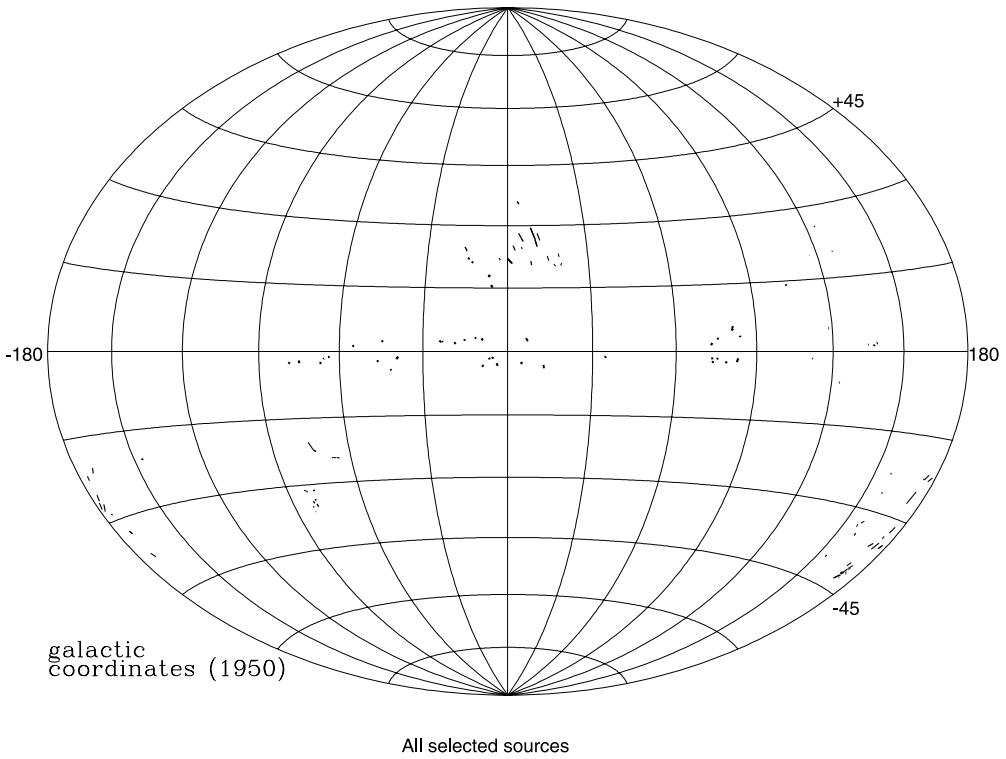

FIG. 2.—Plot of all filaments included in the catalog in Galactic coordinates

complete filament structure in order to put together a catalog of interesting targets; we merely need to be able to identify all bright ridge segments without bias, and the Lindeberg method performs this task well. Moreover, polarization measurements in which two filaments intersect would be ambiguous, and so such regions would have to be omitted from our catalog anyway. The final catalog is a compilation of bright, spatially continuous filaments.

There is a final subtlety built into this algorithm that we have only partially exploited in this project, which might be the basis for further improvements. The process of computing derivatives numerically through finite differencing is stabilized by first smoothing the data with a filter; i.e., by performing an integration (Koenderink 1990). If the filter is a Gaussian, a theorem exists to the effect that no new structure is introduced as the size increases (Lindeberg 1998). This leads to a concept of "scale-space," as it is referred to in the computer vision literature—by running the algorithm at larger and larger filter scales we can construct a hierarchical description of features in the data, with "more important" features visible at the coarser scales. This approach would seem well suited to describing the fractal nature of the cirrus. A qualitative version of the idea is used in Elmegreen, Kim, & Staveley-Smith (2001).

4.2. *Catalog*

This catalog is intended to present a list of potentially useful filaments but not to provide quantitative information on filament signal strength for a particular instrument or measurement technique. For many purposes it is the brightness of the filament above the adjacent background that is of greatest interest. Qualitatively, we have addressed this need by presenting a catalog of bright filaments of high contrast. However, the fractal nature of the cirrus brightness distribution and the variable operating characteristics of individual instruments make a full quantitative discussion of filament brightness and contrast intractable. We suggest that a seeker of suitable filaments use our listing to select bright and long filaments and then examine candidate filaments in the ISSA and Schlegel et al. data to determine the expected signal for their particular instrument.

The nature of Gaussian smoothing combined with our second derivative criteria for filament detection is to achieve maximum sensitivity for filaments on the order of 7′ wide, which is at or near the resolution limit of the *IRAS* detectors at 100 μm. Sensitivity falls off for larger structures, and information is not present in the data for much smaller ones. We still expect that the catalog will provide a useful indicator of bright filaments over a range of width scales. Given the fractal nature of the interstellar cirrus, it is likely that many of our filaments are unresolved and that a detector with higher resolution would measure a higher surface brightness than that seen in the ISSA data.

The physical mechanisms for filament formation have been a matter for much speculation and are connected with larger questions about the overall structure of the interstellar medium (Verschuur 1991). We note that the geometry of the magnetic field around the filament may be more complicated than a simple parallel or perpendicular alignment, as noted in Fiege & Pudritz (2000). Our analysis sets no constraint on the actual nature of the filaments themselves, which hopefully will be elucidated by future polarimetry measurements. In particular, it may be that diffuse filaments are formed by different processes than the brighter, denser ones.

On a related note, adjacent filaments are frequently oriented in the same direction, and a number of circular

shells are clearly seen extending above the Galactic plane in the data before our brightness cuts are made, e.g., the North Polar Spur. An interesting extension to the project would be to correlate these structures with known supershells observed in H I line observations.

Tom Jackson is pleased to acknowledge the mentorship and advice of Michael Werner and T. N. Gautier, who also provided the financial support for his Caltech Summer Undergraduate Research Fellowship. Andrew Lange and Paul Richards provided much assistance and information on the BOOMERanG and MAXIMA missions, respectively. This research was carried out at the Jet Propulsion Laboratory, which is operated by the California Institute of Technology under a contract with NASA.

APPENDIX

CATALOGS OF SELECTED FILAMENTS

The three catalogs (Tables 1, 2, and 3) are presented in the same format. The first three columns in a table give an index number, the ISSA plate on which the filament was detected, and its arc length in arcminutes. The next two columns provide its averaged flux (computed as sum of pixel brightnesses/number of pixels belonging to object) at 100 μm from the data presented in Schlegel et al. (1998) and extrapolated to 340 GHz and expressed as a temperature based on the routines in Finkbeiner et al. (1999), as described in the text. The next eight columns give coordinates for the endpoints and midpoint of the filament. The final columns are the curvature and contrast measures defined above in § 3. Within each catalog, the objects are listed in increasing midpoint right ascension.

TABLE 1
LIST OF FILAMENTS SATISFYING OUR CRITERIA FOR $|b| > 20°$

ID	ISSA Plate	Length (arcmin)	F_{100} (MJy sr^{-1})	ΔT_{340} (mK)	Endpoint 1		Midpoint				Endpoint 2		Curvature	Contrast (deg^{-2})
					α	δ	α	δ	l	b	α	δ		
1.....	430	186.54	8.2	3.2	2 15.8	88 02	2 22.0	88 11	123.79	25.73	2 28.1	88 19	0.76	36.3
2.....	274	18.42	11.4	3.3	2 27.8	16 20	2 28.2	16 25	154.70	−40.01	2 28.3	16 34	0.67	9.8
3.....	273	21.07	11.3	3.3	2 27.7	16 19	2 28.2	16 24	154.72	−40.02	2 28.3	16 35	0.69	9.6
4.....	423	48.67	11.3	3.5	2 44.2	81 53	2 42.7	82 00	127.05	20.31	2 41.6	82 10	0.76	28.1
5.....	274	30.54	10.9	3.3	2 49.7	21 39	2 49.3	21 27	156.88	−33.14	2 49.1	21 10	0.76	22.8
6.....	274	34.16	18.4	7.4	2 53.2	19 16	2 52.9	19 01	159.31	−34.72	2 52.6	18 43	0.81	72.1
7.....	274	56.78	9.6	3.1	2 57.6	21 30	2 55.8	21 30	158.34	−32.28	2 53.9	21 28	0.87	15.2
8.....	239	13.70	12.0	3.2	3 01.8	7 30	3 02.2	7 31	170.60	−42.48	3 02.3	7 38	0.62	13.5
9.....	239	87.77	12.3	3.3	3 04.8	7 38	3 02.3	7 27	170.67	−42.53	2 59.8	7 33	0.71	19.8
10.....	238	87.32	12.3	3.3	3 04.9	7 37	3 02.3	7 26	170.67	−42.53	2 59.8	7 33	0.70	20.2
11.....	238	16.53	11.9	3.2	3 01.8	7 30	3 02.3	7 31	170.61	−42.47	3 02.3	7 39	0.59	13.4
12.....	239	25.86	11.8	3.1	3 04.2	8 10	3 04.9	8 17	170.58	−41.46	3 05.5	8 24	0.69	5.3
13.....	239	22.22	16.0	4.1	3 05.0	7 05	3 04.9	7 13	171.54	−42.26	3 05.0	7 05	0.02	24.6
14.....	239	13.24	16.5	4.3	3 05.3	7 20	3 05.1	7 26	171.38	−42.07	3 05.1	7 32	0.67	23.7
15.....	239	38.59	12.7	3.3	3 06.6	8 10	3 05.3	8 10	170.78	−41.50	3 04.6	7 56	0.67	19.6
16.....	239	10.15	16.0	4.1	3 06.2	7 24	3 06.0	7 22	171.66	−41.98	3 05.6	7 19	0.67	19.3
17.....	239	15.28	15.1	4.0	3 06.8	7 49	3 06.4	7 44	171.44	−41.62	3 05.9	7 41	0.66	23.6
18.....	239	27.86	16.4	4.3	3 07.9	7 32	3 07.7	7 45	171.73	−41.41	3 07.0	7 53	0.68	26.3
19.....	239	62.22	15.6	4.1	3 10.2	8 24	3 08.1	8 17	171.36	−40.93	3 07.0	7 56	0.71	25.4
20.....	239	13.21	14.9	3.9	3 08.0	7 49	3 08.3	7 44	171.89	−41.32	3 08.7	7 41	0.66	15.0
21.....	239	52.16	12.1	3.3	3 09.9	9 59	3 08.4	9 51	170.06	−39.72	3 06.9	9 38	0.77	26.1
22.....	309	30.89	13.0	3.4	3 10.2	26 10	3 10.1	26 27	158.24	−26.36	3 09.6	26 39	0.79	35.7
23.....	239	12.99	12.6	3.4	3 10.3	7 45	3 10.3	7 52	172.27	−40.89	3 10.1	7 57	0.69	16.6
24.....	239	20.63	11.9	3.1	3 11.9	7 09	3 11.4	7 12	173.13	−41.17	3 10.7	7 12	0.73	12.8
25.....	239	50.13	11.6	3.2	3 13.2	8 09	3 12.0	8 04	172.49	−40.45	3 11.0	8 06	0.53	18.4
26.....	239	49.14	11.6	3.2	3 14.1	8 37	3 12.0	8 34	172.14	−40.02	3 10.9	8 27	0.82	28.9
27.....	239	15.09	12.4	3.1	3 12.1	6 45	3 12.4	6 40	173.87	−41.38	3 12.8	6 35	0.69	11.6
28.....	309	31.88	14.9	4.7	3 17.6	29 32	3 17.3	29 45	157.58	−22.74	3 17.1	30 02	0.77	21.9
29.....	239	87.19	17.7	5.1	3 25.8	12 18	3 23.0	12 20	171.27	−35.53	3 20.1	12 28	0.84	22.1
30.....	239	109.42	13.7	3.7	3 33.6	11 03	3 29.9	10 56	174.02	−35.31	3 26.9	10 39	0.78	15.3
31.....	240	31.46	13.1	3.5	3 36.7	12 06	3 35.5	12 05	174.21	−33.54	3 34.8	11 57	0.76	19.2
32.....	240	62.69	12.6	3.3	3 39.5	9 22	3 37.5	9 19	177.04	−35.11	3 35.5	9 15	0.77	18.2
33.....	239	54.23	12.5	3.3	3 39.5	9 21	3 37.7	9 18	177.09	−35.08	3 35.9	9 14	0.82	17.7
34.....	240	82.77	14.3	3.8	3 46.7	12 32	3 43.9	12 22	175.67	−31.87	3 41.6	12 05	0.77	22.4
35.....	204	68.04	14.3	3.3	3 53.4	1 31	3 52.9	0 58	188.03	−37.52	3 52.4	0 25	0.82	27.8
36.....	276	162.35	12.1	3.4	4 01.7	18 12	3 57.0	17 44	173.75	−25.89	3 52.2	17 16	0.77	13.1
37.....	204	45.23	13.6	3.7	4 06.8	4 49	4 06.5	4 26	187.11	−32.72	4 06.1	4 05	0.80	28.1

TABLE 1—*Continued*

ID	ISSA Plate	Length (arcmin)	F_{100} (MJy sr^{-1})	ΔT_{340} (mK)	Endpoint 1		Midpoint				Endpoint 2		Curvature	Contrast (deg^{-2})
					α	δ	α	δ	l	b	α	δ		
38.....	240	42.78	13.8	3.7	4 06.9	4 53	4 06.6	4 32	187.04	−32.64	4 06.0	4 13	0.78	29.8
39.....	276	37.83	16.5	4.7	4 10.4	19 21	4 09.8	19 37	174.51	−22.37	4 09.5	19 55	0.75	18.3
40.....	240	38.63	14.2	4.2	4 11.3	12 44	4 10.9	13 00	180.16	−26.54	4 10.4	13 20	0.75	14.1
41.....	240	38.87	18.6	4.2	4 13.8	8 14	4 13.6	8 33	184.55	−28.83	4 13.0	8 49	0.76	39.3
42.....	276	92.87	14.8	4.2	4 16.7	19 09	4 14.0	19 23	175.41	−21.80	4 10.8	19 19	0.79	13.8
43.....	240	86.24	17.1	4.7	4 16.6	11 32	4 14.2	11 19	182.19	−26.99	4 11.2	11 22	0.81	20.8
44.....	240	111.86	16.4	4.3	4 18.7	10 07	4 15.4	10 23	183.23	−27.35	4 11.5	10 29	0.84	21.3
45.....	276	94.51	13.1	3.9	4 22.0	17 18	4 19.4	17 36	177.77	−22.01	4 16.1	17 42	0.77	16.8
46.....	241	80.77	15.3	4.3	4 23.8	11 28	4 21.1	11 34	183.16	−25.51	4 18.7	11 18	0.76	18.2
47.....	241	50.61	14.3	3.9	4 36.2	13 07	4 34.8	12 55	184.23	−22.03	4 33.1	12 49	0.75	17.0
48.....	241	85.18	15.6	3.7	4 49.7	10 25	4 46.8	10 27	188.22	−21.12	4 44.3	10 40	0.83	16.8
49.....	170	44.25	31.7	8.0	5 36.4	−10 18	5 36.0	−9 57	213.71	−20.69	5 35.5	−9 36	0.77	59.3
50.....	171	43.44	31.9	8.1	5 36.4	−10 18	5 36.0	−9 58	213.72	−20.70	5 35.4	−9 37	0.76	56.1
51.....	15	44.88	15.3	3.3	7 47.3	−74 39	7 47.9	−74 18	286.56	−22.45	7 48.2	−73 57	0.87	26.6
52.....	5	61.10	15.2	3.2	7 47.2	−74 41	7 48.1	−74 12	286.46	−22.41	7 48.7	−73 45	0.83	25.4
53.....	4	113.79	14.1	3.4	7 58.8	−80 21	7 55.2	−80 11	292.67	−24.22	7 51.3	−80 02	0.75	18.9
54.....	15	250.13	14.7	3.0	8 03.1	−71 51	7 57.3	−72 55	285.46	−21.30	7 48.7	−73 44	0.77	35.6
55.....	4	122.74	14.9	3.6	7 59.8	−80 25	8 02.9	−80 54	293.54	−24.20	8 06.6	−81 25	0.79	25.5
56.....	4	127.68	14.1	3.2	8 12.4	−81 38	8 12.7	−82 04	294.86	−24.33	8 18.9	−82 33	0.76	21.5
57.....	149	86.16	30.7	4.0	15 37.4	−24 55	15 34.8	−24 46	344.27	24.28	15 32.1	−24 38	0.76	32.0
58.....	150	31.94	39.5	3.4	15 46.1	−25 43	15 45.0	−25 46	345.45	22.03	15 44.1	−25 51	0.77	20.7
59.....	115	33.54	40.3	3.5	15 46.2	−25 43	15 45.0	−25 46	345.46	22.02	15 44.0	−25 51	0.80	22.4
60.....	149	32.42	40.1	3.4	15 46.2	−25 43	15 45.1	−25 46	345.47	22.02	15 44.1	−25 50	0.78	21.0
61.....	116	32.73	40.3	3.4	15 46.3	−25 43	15 45.2	−25 45	345.50	22.01	15 44.2	−25 50	0.75	20.2
62.....	186	55.24	18.0	4.9	15 53.3	−4 35	15 51.5	−4 40	4.13	35.55	15 49.8	−4 32	0.76	42.6
63.....	222	52.65	18.4	5.0	15 53.3	−4 34	15 51.6	−4 40	4.13	35.53	15 50.0	−4 33	0.76	42.5
64.....	116	31.33	113.7	6.6	15 52.4	−25 46	15 52.2	−25 30	346.94	21.13	15 51.8	−25 16	0.76	102.0
65.....	150	40.03	23.0	3.3	16 18.9	−18 10	16 17.5	−18 10	356.99	21.97	16 16.3	−18 17	0.77	15.5
66.....	187	152.91	20.6	3.0	16 24.8	−9 14	16 19.6	−9 05	5.09	27.32	16 15.1	−9 11	0.79	17.8
67.....	186	86.86	18.6	3.1	16 25.2	−12 45	16 22.4	−12 46	2.34	24.52	16 19.6	−12 39	0.82	13.0
68.....	186	33.36	22.5	3.1	16 25.0	−9 14	16 24.0	−9 12	5.73	26.40	16 22.8	−9 13	0.84	15.0
69.....	187	203.85	15.3	3.1	16 33.2	−5 34	16 26.9	−5 17	9.77	28.11	16 20.6	−5 09	0.78	20.9
70.....	223	203.54	15.3	3.1	16 33.2	−5 35	16 26.9	−5 17	9.78	28.11	16 20.6	−5 10	0.77	20.9
71.....	150	97.30	24.6	5.5	16 31.5	−15 43	16 28.6	−15 56	0.66	21.37	16 25.3	−15 58	0.79	23.2
72.....	187	35.32	25.6	3.6	16 30.1	−10 34	16 28.8	−10 33	5.31	24.64	16 27.9	−10 40	0.81	15.2
73.....	187	116.72	24.3	5.5	16 32.4	−15 32	16 29.1	−15 54	0.77	21.29	16 25.2	−16 00	0.76	23.7
74.....	151	120.94	24.2	5.5	16 32.7	−15 29	16 29.4	−15 54	0.83	21.24	16 25.2	−15 58	0.76	23.8
75.....	223	118.66	16.0	3.5	16 37.6	−4 26	16 34.3	−4 08	12.01	27.25	16 30.2	−4 05	0.77	29.3
76.....	187	105.39	19.0	4.0	16 40.1	−6 03	16 36.9	−5 48	10.88	25.76	16 33.4	−5 39	0.80	17.6
77.....	223	110.86	19.0	4.0	16 40.3	−6 04	16 37.0	−5 48	10.88	25.76	16 33.3	−5 38	0.80	17.0
78.....	187	72.53	22.6	5.5	16 50.5	−10 22	16 49.3	−9 59	9.00	20.87	16 46.4	−9 57	0.75	13.3
79.....	224	73.60	13.7	3.6	16 59.9	−4 49	16 58.0	−4 32	15.17	22.05	16 55.3	−4 33	0.76	19.2
80.....	223	51.35	11.2	3.2	17 04.7	−1 10	17 03.1	−1 03	19.11	22.78	17 01.4	0 55	0.76	20.9
81.....	224	42.91	12.0	3.5	17 09.3	−3 34	17 07.9	−3 34	17.44	20.47	17 06.6	−3 43	0.80	13.5
82.....	224	42.04	13.1	3.9	17 12.5	−1 51	17 12.1	−1 32	19.87	20.60	17 11.5	−1 13	0.75	16.4
83.....	429	40.29	9.4	3.3	22 14.4	80 50	22 13.0	80 43	116.80	20.06	22 11.8	80 37	0.83	46.6

Notes.—Right ascension and declination (α and δ) are given for the B1950 equinox; units of right ascension are hours, minutes, and seconds, and units of declination are degrees, arcminutes, and arcseconds. Galactic longitude and latitude (l and b) have units of degrees.

TABLE 2

List of Filaments Satisfying Our Criteria for $|b| < 20°$

ID	ISSA Plate	Length (arcmin)	F_{100} (MJy sr^{-1})	ΔT_{340} (mK)	Endpoint 1		Midpoint				Endpoint 2		Curvature	Contrast (deg^{-2})
					α	δ	α	δ	l	b	α	δ		
84.....	408	48.26	369.8	36.9	0 05.2	67 01	0 03.8	66 57	118.59	4.75	0 02.0	66 56	0.76	57.8
85.....	390	34.83	292.9	38.5	0 51.5	56 19	0 50.4	56 18	123.20	−6.31	0 49.2	56 17	0.92	84.0
86.....	391	41.93	132.7	12.1	2 31.1	61 36	2 30.0	61 40	134.69	1.38	2 28.4	61 42	0.76	58.3
87.....	391	58.53	235.0	28.9	2 49.8	60 32	2 48.0	60 31	137.15	1.21	2 46.0	60 30	0.83	70.9
88.....	391	47.16	388.7	57.3	3 00.0	60 13	2 58.3	60 17	138.38	1.60	2 56.9	60 24	0.76	79.8
89.....	32	62.35	194.5	37.8	9 57.5	−57 42	9 55.6	−57 43	281.48	−2.54	9 53.4	−57 45	0.85	44.3
90.....	32	40.52	209.4	28.0	10 20.0	−59 20	10 19.6	−59 37	285.12	−2.29	10 18.5	−59 52	0.75	52.0

TABLE 2—*Continued*

ID	ISSA Plate	Length (arcmin)	F_{100} (MJy sr^{-1})	ΔT_{340} (mK)	Endpoint 1		Midpoint				Endpoint 2		Curvature	Contrast (deg^{-2})
					α	δ	α	δ	l	b	α	δ		
91.....	33	41.39	106.0	18.9	11 18.7	−63 08	11 17.7	−63 21	292.98	−2.54	11 17.4	−63 40	0.77	20.0
92.....	33	46.18	339.4	45.2	11 32.0	−62 50	11 30.7	−62 53	294.22	−1.63	11 29.0	−62 56	0.80	30.6
93.....	34	79.74	207.4	35.7	11 50.8	−63 09	11 48.2	−63 05	296.19	−1.28	11 45.5	−62 58	0.77	13.2
94.....	34	69.37	239.4	25.7	13 08.2	−61 09	13 06.0	−61 16	305.05	1.26	13 03.7	−61 22	0.77	19.2
95.....	35	36.18	132.2	20.6	14 25.4	−58 07	14 24.6	−57 52	315.46	2.40	14 24.3	−57 38	0.75	14.2
96.....	35	36.50	141.5	19.7	14 27.1	−62 59	14 26.7	−62 44	313.93	−2.22	14 25.5	−62 33	0.77	19.1
97.....	36	48.97	216.4	36.7	15 11.7	−62 33	15 10.0	−62 33	318.48	−4.26	15 08.5	−62 31	0.84	68.4
98.....	36	62.05	383.1	47.5	15 15.9	−58 30	15 14.6	−58 54	320.86	−1.43	15 13.7	−59 21	0.77	49.4
99.....	59	67.87	153.4	19.4	16 20.4	−46 17	16 18.1	−46 19	336.16	2.42	16 16.0	−46 27	0.80	19.3
100.....	150	40.68	400.0	30.8	16 21.1	−23 51	16 20.7	−23 33	353.22	17.85	16 20.3	−23 12	0.79	55.2
101.....	86	36.97	144.6	17.8	16 23.1	−45 52	16 22.0	−45 49	336.98	2.31	16 20.7	−45 46	0.79	14.4
102.....	150	47.23	121.4	22.2	16 33.0	−24 27	16 31.4	−24 29	354.17	15.40	16 29.9	−24 29	0.84	47.8
103.....	116	47.18	120.4	22.0	16 33.0	−24 28	16 31.5	−24 29	354.18	15.39	16 29.8	−24 29	0.89	49.1
104.....	86	35.06	298.8	34.7	16 40.5	−42 33	16 40.2	−42 50	341.39	1.95	16 39.8	−43 07	0.78	37.2
105.....	87	32.57	146.9	12.5	16 49.9	−39 51	16 49.0	−39 46	344.80	2.67	16 47.9	−39 42	0.78	21.8
106.....	87	42.09	115.3	13.6	17 00.3	−36 14	16 59.3	−36 24	348.69	3.21	16 58.3	−36 41	0.75	17.3
107.....	87	36.29	124.1	14.1	17 07.8	−35 05	17 07.5	−34 46	351.00	2.86	17 07.0	−34 31	0.75	16.4
108.....	117	36.69	121.6	13.8	17 07.7	−35 04	17 07.5	−34 45	351.02	2.87	17 07.2	−34 30	0.81	17.0
109.....	118	31.92	191.9	25.6	17 33.7	−35 17	17 32.7	−35 13	353.58	−1.64	17 31.6	−35 16	0.77	15.2
110.....	87	38.16	138.7	15.3	17 34.3	−38 27	17 34.1	−38 08	351.27	−3.44	17 33.4	−37 53	0.80	13.6
111.....	87	37.08	202.7	25.4	17 35.4	−34 32	17 35.1	−34 14	354.66	−1.50	17 34.5	−33 58	0.77	17.1
112.....	87	58.04	146.0	16.1	17 47.4	−33 44	17 45.4	−33 49	356.16	−3.10	17 43.7	−33 42	0.78	36.6
113.....	153	63.02	107.1	13.8	17 49.5	−21 36	17 47.6	−21 44	6.75	2.74	17 45.6	−21 47	0.77	14.2
114.....	118	40.67	196.1	19.7	18 05.4	−26 11	18 04.0	−26 10	4.79	−2.74	18 02.8	−26 06	0.83	20.3
115.....	153	53.74	105.0	10.9	18 25.3	−19 46	18 23.7	−19 38	12.73	−3.60	18 22.0	−19 31	0.77	15.1
116.....	227	30.03	357.4	57.9	18 56.2	1 01	18 56.2	0 46	34.52	−1.26	18 56.5	0 33	0.75	21.6
117.....	331	42.91	157.6	26.5	20 07.2	35 26	20 06.9	35 46	73.08	1.65	20 06.4	36 06	0.79	29.2
118.....	360	34.82	117.0	15.2	20 08.5	38 10	20 08.3	38 26	75.46	2.87	20 08.0	38 41	0.77	21.8
119.....	385	42.16	141.1	16.8	20 14.1	44 11	20 13.6	44 29	81.07	5.38	20 13.6	44 52	0.85	26.0
120.....	361	47.49	168.2	20.3	20 16.9	44 10	20 15.4	44 05	80.91	4.89	20 13.8	44 02	0.85	25.0
121.....	360	44.89	167.8	20.3	20 16.8	44 10	20 15.5	44 05	80.93	4.88	20 14.0	44 00	0.75	25.6
122.....	385	40.57	165.0	20.0	20 16.9	44 10	20 15.6	44 05	80.94	4.87	20 14.2	44 04	0.78	26.2
123.....	332	40.50	105.9	21.3	20 21.5	34 07	20 20.3	34 09	73.27	−1.53	20 18.9	34 06	0.79	13.8
124.....	331	30.48	119.4	21.6	20 24.2	34 05	20 24.0	33 52	73.48	−2.32	20 23.7	33 36	0.83	28.0
125.....	332	33.64	120.5	21.7	20 24.4	34 07	20 24.1	33 52	73.49	−2.34	20 23.9	33 35	0.77	28.7
126.....	332	31.52	200.1	30.8	20 26.5	35 28	20 26.3	35 43	75.27	−1.63	20 26.1	35 59	0.87	26.0
127.....	385	31.15	323.5	59.8	20 31.0	45 31	20 31.9	45 28	83.74	3.31	20 33.0	45 26	0.81	97.0
128.....	361	31.87	174.0	22.0	20 39.1	37 35	20 39.0	37 53	78.52	−2.35	20 39.1	38 06	0.84	12.8
129.....	361	65.34	188.7	27.1	20 51.9	40 55	20 51.0	41 22	82.69	−1.95	20 50.4	41 54	0.77	24.3
130.....	420	64.30	176.0	40.0	21 03.4	67 57	21 01.3	67 57	104.07	14.16	20 59.1	67 55	0.77	103.5
131.....	389	37.74	113.4	16.9	23 20.5	59 12	23 19.3	59 12	111.74	−1.43	23 18.0	59 10	0.80	26.4

Notes.—Right ascension and declination (α and δ) are given for the B1950 equinox; units of right ascension are hours, minutes, and seconds, and units of declination are degrees, arcminutes, and arcseconds. Galactic longitude and latitude (l and b) have units of degrees.

TABLE 3

List of Filaments Satisfying Our Criteria for the Large Magellanic Cloud

ID	ISSA Plate	Length (arcmin)	F_{100} (MJy sr^{-1})	ΔT_{340} (mK)	Endpoint 1		Midpoint				Endpoint 2		Curvature	Contrast (deg^{-2})
					α	δ	α	δ	l	b	α	δ		
132.....	13	16.18	23.8	4.4	4 52.6	−67 21	4 52.6	−67 14	278.20	−36.26	4 52.4	−67 06	0.78	126.2
133.....	13	120.13	28.9	5.6	5 06.6	−69 07	5 02.4	−69 07	280.14	−34.88	4 58.6	−69 06	0.89	79.5
134.....	13	22.07	19.1	3.6	5 04.4	−67 41	5 04.3	−67 31	278.19	−35.09	5 04.0	−67 20	0.83	78.0
135.....	13	16.62	18.8	3.6	5 04.7	−67 03	5 04.4	−67 08	277.75	−35.17	5 04.1	−67 16	0.77	81.9
136.....	13	94.77	22.4	4.3	5 16.3	−68 20	5 12.8	−68 23	279.01	−34.13	5 10.0	−68 30	0.77	40.8
137.....	13	55.94	70.9	13.6	5 18.5	−69 24	5 16.8	−69 22	280.09	−33.58	5 14.8	−69 23	0.77	93.3
138.....	13	28.24	53.8	10.3	5 41.2	−70 33	5 40.8	−70 23	280.91	−31.39	5 40.0	−70 13	0.79	75.5
139.....	13	21.99	36.1	6.9	5 41.2	−70 35	5 41.0	−70 44	281.32	−31.33	5 41.2	−70 56	0.87	53.4
140.....	13	48.98	16.4	3.1	5 43.1	−67 55	5 41.5	−67 55	278.02	−31.55	5 39.9	−67 53	0.77	50.0
141.....	13	66.06	18.1	3.5	5 46.0	−67 01	5 44.8	−67 26	277.44	−31.27	5 43.9	−67 51	0.77	77.9

Notes.—Right ascension and declination (α and δ) are given for the B1950 equinox; units of right ascension are hours, minutes, and seconds, and units of declination are degrees, arcminutes, and arcseconds. Galactic longitude and latitude (l and b) have units of degrees.

REFERENCES

Appleton, P. N., Siqueira, P. R., & Basart, J. P. 1993, AJ, 106, 1664
Beck, R., Brandenburg, A., Moss, D., Shukurov, A., & Sokoloff, D. 1996, ARA&A, 34, 155
Beichman, C. A., Neugebauer, G., Habing, H. J., Clegg, P. E., & Chester, T. J. 1988, *IRAS* Catalogs and Atlases. Volume 1: Explanatory Supplement (NASA RP-1190; Washington: GPO)
Clemens, D. P., et al. 2000, BAAS, 196, 25.08
Elmegreen, B. G., Kim, S., & Staveley-Smith, L. 2001, ApJ, 548, 749
Fiege, J. D., & Pudritz, R. E. 2000, ApJ, 544, 830
Finkbeiner, D. P., Davis, M., & Schlegel, D. J. 1999, ApJ, 524, 867
Gautier III, T. N., Boulanger, F., Pérault, M., & Puget, J. L. 1992, AJ, 103, 1313
Hildebrand, R. H., Davidson, J. A., Dotson, J. L., Dowell, C. D., Novak, G., & Vaillancourt, J. E. 2000, PASP, 112, 1215
Koenderink, J. J. 1990, Solid Shape (Cambridge: MIT Press)
Laureijs, R. J., Lemke, D., & Liljeström, T. 1994, in ASP Conf. Ser. 58, First Symp. on the Infrared Cirrus and Diffuse Interstellar Clouds, ed. R. M. Cutri & W. B. Latter (San Francisco: ASP), 150
Lazarian, A., & Draine, B. T. 2000, ApJ, 536, L15
Leitch, E. M., Readhead, A. C. S., Pearson, T. J., & Myers, S. T. 1997, ApJ, 486, L23
Lindeberg, T. 1996, Technical Report ISRN KTH NA/P-96/18-SE (Stockholm: Royal Inst. Tech.)
———. 1998, Int. J. Comput. Vision, 30, 79
López, A. M., Lumbreras, F., Serrat, J., & Villanueva, J. J. 1999, IEEE Trans. Pat. Anal. and Machine Intelligence, 21, 327
Masi, S., et al. 2001, ApJ, 533, L93
Novak, G., Davidson, J. A., Dragovan, M., & Hildebrand, R. H. 1999, BAAS, 31, 1001
Schlegel, D. J., Finkbeiner, D. P., & Davis, M. 1998, ApJ, 500, 525
Verschuur, G. L. 1991, Ap&SS, 185, 305
———. 1994, in ASP Conf. Ser. 58, First Symp. on the Infrared Cirrus and Diffuse Interstellar Clouds, ed. R. M. Cutri & W. B. Latter (San Francisco: ASP), 184
Wheelock, S. L., et al. 1994, *IRAS* Sky Survey Atlas: Explanatory Supplement (JPL Publ. 94-11; Pasadena: JPL)
Zweibel, E. G. 1996, in ASP Conf. Ser. 97, Polarimetry of the Interstellar Medium, ed. W. G. Roberge & D. C. B. Whittet (San Francisco: ASP), 486

Note added in proof.—Dr. J. Bregman of the Ames Research Center has kindly informed us that inspection of the Digital Sky Survey images shows that, particularly at low Galatic latitude, a number of the filaments in our catalog appear to be bright rims on dark clouds or at the edge of H II regions. This reinforces the recommendation made in § 4.2 above that users of the catalog inspect the filaments they select to be certain that they are appropriate for a particular application.